Hindawi Publishing Corporation
International Journal of Aerospace Engineering
Volume 2011, Article ID 896836, 15 pages
doi:10.1155/2011/896836

Research Article

Argon 4*s* and 4*p* Excited States Atomic Data Applied in ARC-JET Modeling

K. Katsonis,[1] Ch. Berenguer,[1,2] A. Kaminska,[3] and M. Dudeck[4]

[1] *Centre de Données Atomiques GAPHYOR, Laboratoire de Physique des Gaz et des Plasmas, UMR 8578, Université de Paris XI, 91405 Orsay, France*
[2] *DEDALOS, 32 rue Charles de Gaulle, 91400 Orsay, France*
[3] *Institute of Electric Power Engineering, IEPE, Poznan University of Technology, 60-965 Poznan, Poland*
[4] *Institut Jean Le Rond d'Alembert, Université de Paris VI, 75252 Paris Cedex 05, France*

Correspondence should be addressed to K. Katsonis, konstantinos.katsonis@u-psud.fr

Received 8 March 2011; Revised 31 May 2011; Accepted 16 June 2011

Academic Editor: I. D. Boyd

Evaluated atomic data concerning the 4*s* and 4*p* configurations of Ar I are averaged in order to simplify their use in various cases of Ar plasma modeling and diagnostics. These data are used here to model a low-power arcjet, running with Argon at low pressure. In so doing, they are explicitly introduced in the chemical processes included in a fluid Navier-Stokes type code, allowing for evaluation of the spectroscopically measurable level populations and of the electronic temperatures. The characteristics of the model are described and the main processes are discussed in view of the results of the calculations.

1. Introduction

We address the important problem of the presence of species in excited states in plasmas frequently studied in aerospace engineering. This fact contributes significantly to the overall plasma properties and therefore it has to be considered in the corresponding modeling and diagnostics. Indeed, due to the available energy, the different species are not expected to be in their ground state only; many excited levels of neutral and ionized species are definitely present in the plasma. The analysis of the population of the various excited species reveals a great interest for several domains. Mainly, excited levels of a neutral species, atom or molecule, can play an important role in the ionization process. Moreover, calculation of the different levels population is necessary to evaluate the emission spectra and to allow a spectroscopic validation of the model. Besides, inclusion of a few molecular levels can be used to estimate a "pseudo" vibrational temperature generally obtained by the ground state and the first level. The level of coupling between microscopic and macroscopic description has to be examined for each case. Here, in order to illustrate the importance of the excited states, a first study has been carried out with Argon as feeding gas for a D.C. low-pressure arcjet. The production rates (mainly electron collision excitation and ionization) and the transition probabilities leading to de-excitation of the main excited levels have been evaluated by the GAPHYOR team, using a big number of theoretical codes and also experimental data, as described in Section 3, after a description of the neutral Argon structure in Section 2. Note that these data can be useful for diagnostics of various plasmas, after adding a small quantity of Ar as a tracer gas.

The study of arcjets is selected here to illustrate the use of the Ar I atomic data, because of their importance in many aerospace applications. Space missions aiming at the exploration of the Solar System planets, notably Mars, Venus, and Saturn, often present a hypersonic flight through a particular planetary atmosphere for a trajectory chosen for its aerobreaking or aerocapture properties before landing. These trajectories induce many complex phenomena due to the presence of a strong frontal shock wave, as molecule dissociation in the ambient gas, ionization. and radiation. These phenomena are related to a context of nonequilibrium conditions (chemical and ionization in nonequilibrium situation, non-Maxwellian electron distribution,

nonequilibrium between the kinetic, electronic, vibrational, and rotational temperatures T, T_e, T_{vj}, T_{rj}, lack of Boltzmann equilibrium between the populations of the different states). All these phenomena contribute to a considerable energy transfer onto the spacecraft surface. A precise knowledge of this energy is necessary to define and optimize the thermal protection system (TPS) of the spacecraft. The objective is a minimization of the weight of the TPS in order to lower the cost of the mission maintaining a sufficient quality of security for the required restricting trajectories.

The simulation of the plasma conditions, appearing around a spacecraft during its hypersonic entry in a planetary atmosphere, is based on various ground test facilities such as shock tubes, microwave plasma sources, inductively coupled torches (ICP), and arcjets. Each plasma source exhibits specific advantages and disadvantages. The main advantage of the arcjets consists in their ability to sustain a low-pressure plasma flow of large size (around 1 m for a few hours) with electron properties similar to the flight spacecraft conditions, even if the energy exchange differs from that of a shock wave (arc-gas exchange) and the Mach number is generally low (limited to a value around 4-5). Arcjets are currently considered as one of the most powerful tools for the study of reentry plasmas.

Among the other various aerospace applications of arcjets we mention their use in space propulsion.

For an arcjet running at reduced pressure (described in Section 4) being of interest here, a model based on the Navier-Stokes equations, using a finite-difference scheme, was developed at the Institute of Electric Power Engineering (IEPE) of the Poznan University of Technology. It takes into account arc-coupling effects, dissipative effects (gas viscosity, diffusion of the species, heat transfer, electron mobility), and ionization processes. We are here reporting on results introducing a thermal nonequilibrium (T, T_e) as applied to an Argon plasma flow. In the plasma description electrons and chemical species (atoms and molecules, both neutral and ionized) are explicitly present. As potential sheaths near the surfaces are not introduced and the local scale of description is also bigger than the Debye length, a local electron neutrality condition including all the charged species is assumed throughout. Consequently, the electronic density n_e is everywhere, the same with the Ar^+ density.

The plasma flow parameters inside an arcjet (electron density, electron temperature, pressure, and heavy particle temperature along the arcjet axis) obtained from the Navier-Stokes model (code Papyrus) available in IEPE is determined and the electron density is compared to its calculation pertaining to equilibrium condition. Moreover, the populations of Ar(4s) and Ar(4p) are calculated from the plasma density and from the neutral concentration, for a set of processes (electron collisions and radiative deexcitations). Knowledge of the coefficients of the specific excitation and ionization reaction rates allowed for calculation of these two populations. This has been done on different points along the arcjet axis and for different arc intensities. The result of the main processes involving these two states has been evaluated from our calculations and presented in Section 5.

2. Properties of the Two Ar(4s) and Ar(4p) Levels

The 4s and 4p Ar I levels are among the most extensively studied rare gas levels, due to their intrinsic physical properties and because they generate spectral lines frequently present in various applications, both in the visible (4s–4p) and in the UV regions (3p–4s). Their importance in the whole excited level system of Ar I can be appreciated by inspection of the Grotrian diagram of Ar I given in Figure 1. The levels belonging to the core $^2P_{3/2}$ ($j_c = 3/2$, unprimed) are represented in black on the right part of the diagram and the levels of the core $^2P_{1/2}$ ($j_c = 1/2$, primed) in blue in the left part of the diagram. The metastable, transitory and quasimetastable levels are marked in red by m, t, and q-m correspondingly. Two red arrows indicate the allowed radiative transitions to the ground level (GL) from the 4s transitory levels, while the two black arrows crossed out correspond to forbidden transitions from the 4s metastable levels.

Of the four 4s levels (two with $j_c = 3/2$ and two with $j_c = 1/2$ in jK coupling description) two are transitory and two metastable, the transitions of the latter to the GL being forbidden and difficult to observe in experimental plasmas. This fact contributes to an increased population of these levels in comparison with most excited states, to the point that their population cannot be neglected in comparison with the population of the GL. The ionization cross sections of the excited states being considerably higher than the one of the GL, the metastable 4s levels, even less populated than the GL, may significantly contribute to the overall plasma ionization.

The ten 4p Ar I levels (six with $j_c = 3/2$ and four with $j_c = 1/2$) cannot directly decay to the 3p ground level, a fact that contributes to somehow increase their population, although all of them can easily decay to the lower-situated 4s levels through sixteen jK allowed transitions [1]. These constitute the well-known stronger Ar "red" lines around 800 nm (followed in intensity by the "blue" lines coming from the 4s–5p transitions) which significantly contribute to the 4s levels population. Seven among them lead to the two metastable 4s levels. Among the lower 4p levels ($2p_{10}$, $2p_9$, $2p_6$ in the Paschen notation), the first and the last one decay almost one order of magnitude easier to the metastable $1s_5$ than to the transitory $1s_4$. Also, the $2p_9$ decays practically only to the metastable $1s_5$. These facts confer a quasimetastable character to the three $2p_{10}$, $2p_9$, and $2p_6$ levels marked by red circles in Figure 1. Notations according to the empirical Paschen scheme have also been used here because they illustrate the sequential position of the levels in the Ar Grotrian diagram. Interestingly, in the often used LS coupling description, there is a strong mixing of the two transitory 4s levels $^3P_1$ ($[3/2]_1$) and $^1P_1$ ($[1/2]_1$) ($1s_4$ and $1s_2'$ correspondingly in the Paschen notation) and of the 4p $^3D_1$ ($[3/2]_1$, $2p_7$), $^1P_1$ ($[3/2]_1$, $2p_4'$) and $^3P_0$ ($[1/2]_0$, $2p_5$), $^1S_0$ ($[1/2]_0$, $2p_1'$) levels.

A complete description of the GL and the 14 lower excited levels is given in Table 1. It includes, from the left to the right columns, the level index (i) going from

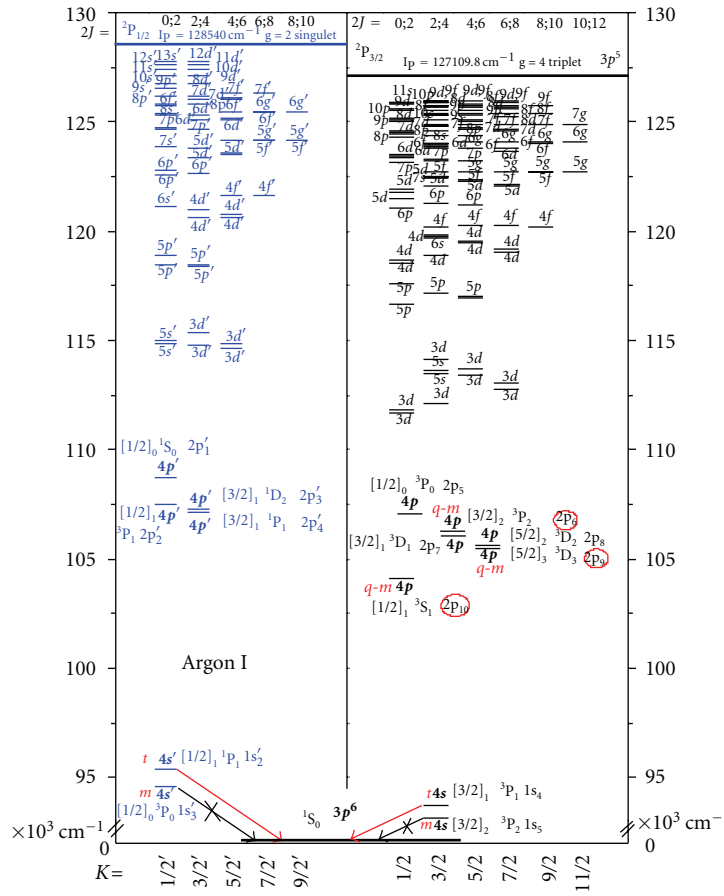

Figure 1: Grotrian diagram of Ar I.

Table 1: List of the 15 lower energy levels of Ar I.

i	c/c	n	l	jK	LS	P.N.	J	g	E. exp.	Char.
1	$3p$	3	1		$^1S_0$		0	1	0.000	
2	$4s$	4	0	$[3/2]_2$	$^3P_2$	$1s_5$	2	5	93143.7600	m
3	$4s$	4	0	$[3/2]_1$	$^3P_1$*	$1s_4$	1	3	93750.5978	t
4	$4s'$	4	0	$[1/2]_0$	$^3P_0$	$1s'_3$	0	1	94553.6652	m
5	$4s'$	4	0	$[1/2]_1$	$^1P_1$*	$1s'_2$	1	3	95399.8276	t
6	$4p$	4	1	$[1/2]_1$	$^3S_1$	$2p_{10}$	1	3	104102.0990	q-m
7	$4p$	4	1	$[5/2]_3$	$^3D_3$	$2p_9$	3	7	105462.7596	q-m
8	$4p$	4	1	$[5/2]_2$	$^3D_2$	$2p_8$	2	5	105617.2700	
9	$4p$	4	1	$[3/2]_1$	$^3D_1$¤	$2p_7$	1	3	106087.2598	
10	$4p$	4	1	$[3/2]_2$	$^3P_2$	$2p_6$	2	5	106237.5518	q-m
11	$4p$	4	1	$[1/2]_0$	$^3P_0$°	$2p_5$	0	1	107054.2720	
12	$4p'$	4	1	$[3/2]_1$	$^1P_1$¤	$2p'_4$	1	3	107131.7086	
13	$4p'$	4	1	$[3/2]_2$	$^1D_2$	$2p'_3$	2	5	107289.7001	
14	$4p'$	4	1	$[1/2]_1$	$^3P_1$	$2p'_2$	1	3	107496.4166	
15	$4p'$	4	1	$[1/2]_0$	$^1S_0$°	$2p'_1$	0	1	108722.6194	

i: level index.
c/c: configuration and core description.
jK description from NIST, LS description from our CbA calculations.
Unprimed for core $^2P_{3/2}$, primed for core $^2P_{1/2}$.
Symbols *, ¤, ° denote the most strongly mixed levels; all the levels with the same J within a same configuration are mixed.
P.N.: Paschen notation.
E. exp.: experimental energy from NIST in cm^{-1}.
Char.: character of the level: transitory/metastable/quasimetastable.

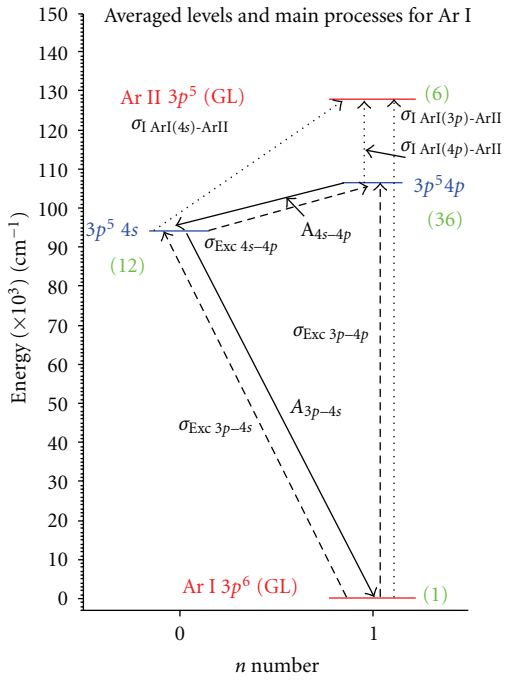

Figure 2: Grotrian diagram for averaged levels of Ar I and Ar II.

1 to 15, the configuration and core description (c/c), the n and l quantum numbers, the jK and LS terms descriptions, the Paschen notation (P.N.), the J quantum number, the statistical weight g, the experimental energies taken from NIST (http://www.physics.nist.gov/cgi-bin/AtData/main_asd/), and the character of the level (Char). As in Figure 1, the unprimed levels belong to the core $^2P_{3/2}$ and the primed ones to the core $^2P_{1/2}$. Symbols $*$, ¤, $\circ$ denote the most strongly mixed levels, but in a general way all the levels having the same J are somehow mixed. We averaged those 15 levels into three global levels: GL, 4s, and 4p.

The next lower Ar I excited levels belong to the 3d, 5s, and 5p configurations. The first of them gives the important lines of the 3d–4p multiplet, which lie in the red-infrared spectral region, as expected in view of the small distances between their levels appearing in the configurations shown in the Grotrian diagram of Figure 1. The last of the aforementioned configurations, the 5p, results in the very important "blue" lines of the 4s–5p multiplet. These are the most intense nonresonant lines observed in the Ar I spectrum after the "red" ones. The relative intensities of the "blue" versus the "red" lines give a first evaluation of the plasma electronic temperature T_e.

It becomes evident that if we seek a better consideration of the important atomic processes present in re-entry studies and other arcjet applications, we have to include in the models at least a collective representation of the four 4s and ten 4p levels situated between the neutral Ar I GL and the ion Ar II ones. Note that it is possible to further separate the metastable from the transitory levels and add the averaged 3/4d configurations. However, the mean values of the atomic processes concerning a simplified "four levels" atomic model

Table 2: Averaged energy levels of Ar I, II and their statistical weights.

conf.	n	l	g	Energy
$3p^6$	3	1	1	0.000
4s(m)	4	0	6	93378.7442
4s(t)	4	0	6	94575.2127
4s	4	0	12	93976.9785
4p	4	1	36	106227.5353
3d	3	2	60	113606.4010
$3p^5$	3	1	6	127586.9944

conf.: configuration.
Energy: averaged energy in cm^{-1}.
All the energies are from the ground level of Ar I.

(consisting of the Ar I GL, its continuum represented by the average of the two Ar II GL and the two global excited 4s and 4p levels) have been used here. They are calculated from data corresponding to the 14 individual 4s and 4p levels and to the two Ar II GL. The global levels of Ar I which are used here are schematically shown in Figure 2. In the bottom we see in red the $3p^6$ level, which is a real level, as there is only one core for Ar I GL. In the upper part, averaged 4s and 4p levels are represented in blue. The averaged GL of Ar II is also shown in red. Its energy has been calculated from the two GLs of Ar II shown in the detailed Grotrian diagram of Figure 1. All global statistical weights are given in green into parenthesis. Arrows show the main processes, excitation (dashed arrows), radiative de-excitation (plain arrows), and ionization (dotted arrows). A list of the averaged energy levels, including more global levels than those used here, is given in Table 2. This table contains the characteristics of seven averaged levels, $3p^6$ (GL Ar I), 4s(m), 4s(t), 4s, 4p, 3d, and $3p^5$ (GL Ar II). We give the configurations, the n and l quantum numbers, the statistical weights, and the energies from averaging experimental ones on the statistical weight of each individual data.

3. Atomic Data Evaluation

We have made extensive calculations and a detailed evaluation of both Einstein transition probabilities (A_{ij}) and electron collision excitation cross sections (σ_{exc}) concerning the 4s and 4p Ar I levels and also those constituting the next configurations 3/4d, 5s, and 5p [2]. Thus, recommended values for the data needed in various applications have been obtained. These are valid in both the low- and high-energy regions. The choice of the processes was made considering the fact that spontaneous emission and inelastic electron collisions are fundamental not only for modeling purposes, but also because they essentially define the plasma spectra that are used both to diagnose the plasma and to validate the models. Special attention was given to the 4s and 4p/5p configurations because, as mentioned, they concern the well-known "red" and "blue" main Ar I spectral lines [3, 4].

Considering the better experimental knowledge of the energy levels, more transition probabilities calculations have been made in GAPHYOR for Ar I, using a code (CbA)

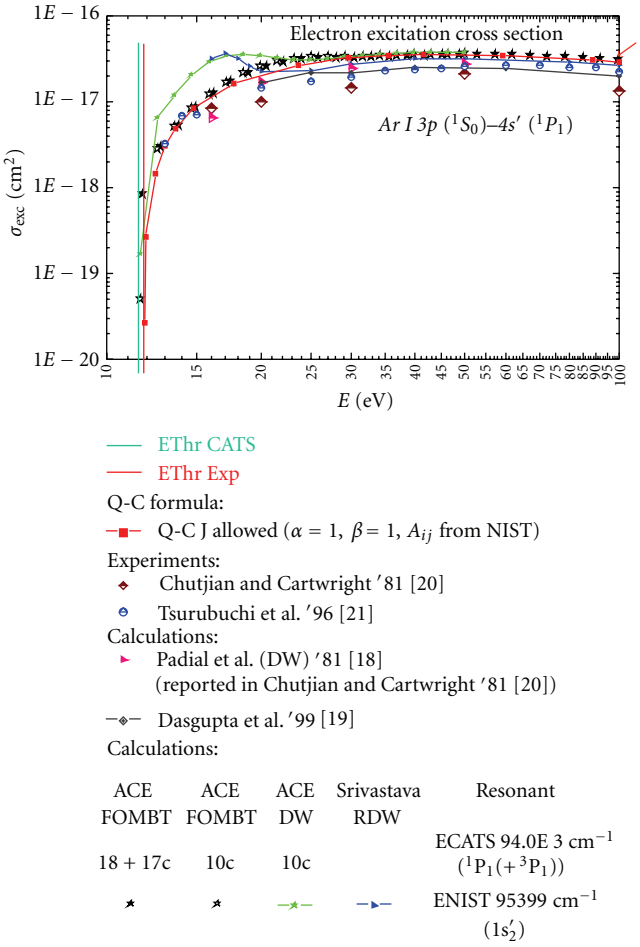

FIGURE 3: Electron excitation cross section of Ar I $3p$ ($^1S_0$)–$4s'$ ($^1P_1$).

based in the Coulomb approximation, proposed by Bates and Damgaard [5], both in *jK* and *LS* coupling formulations. The *jK* coupling has given better results for Ar I, thus confirming our previous choice in using *jK* coupling description for the neutral rare gases Ne, Ar, Kr, and Xe calculations (see, e.g., [1] for the Ar case). These data were compared with new intermediate coupling results from the SUPERSTRUCTURE code [6] and from CATS, a Cowan code as adapted by Abdallah Jr. et al. [7], available from LANL (http://aphysics2.lanl.gov/tempweb/). Experimental results were also obtained in the University of Ioannina [8] and compared to previous results described in the paper "Important Atomic Spectra" contained in the "*American Institute of Physics Handbook*" [9].

The excitation cross section evaluations of the GL to the $4s$ and $4p$ levels of Ar I and of $4s$ to $4p$ ones were based on calculations with various types of approximations—Distorted Wave (DW), born, relativistic distorted wave (RDW) and first order many body theory (FOMBT)—in comparison with the existing experiments and with results from quasiclassical formulas [3, 4, 10, 11]. The latter were initially proposed by Drawin [12], both for the electron collision ionization and for the excitation of the neutral atoms, on the basis of previous studies by Gryziński [13] of the three-body problem. Lately, these quasiclassical formulas were extended after performing numerical solutions of the few body problem in the Classical Trajectory Monte Carlo (CTMC) approximation [14, 15]. The low energy asymptotic values of excitation cross sections given by these formulas have been proved conformal to the low-energy variation laws (see, e.g., [16]). In the high-energy region, the energy variation is conformal to the Born approximation, which is also valid for our DW and FOMBT results.

A typical evaluation result for the GL electronic excitation cross-section $3p$ ($^1S_0$)–$4s'$ ($^1P_1$) in the energy range from threshold to 100 eV is given in Figure 3. The theoretical threshold obtained by CATS being notably lower than the experimental one, the corresponding FOMBT and DW cross sections shown are eventually displaced in the evaluation to adapt them to the real threshold. For the transition of Figure 3, results obtained with a set of 18 outer shell and 17 inner shell configurations (18 + 17c) are near to those obtained with a set of only ten outer shell configurations (10c). In this case, increasing the number of configurations in the calculations does not change the results significantly. DW approximation gives higher values in the near threshold region than FOMBT. We present also RDW results [17] which are quite similar in the high-energy region where relativistic effects are expected. Available theoretical data from [18, 19] are also included. The Q-C formula results shown in the figure use transition probability values from NIST. Theoretical results are compared to two available experimental sets [20, 21]. For the transition studied here, experimental results are in rather good agreement with theoretical ones. Similar evaluations have been made for the remaining three transitions of the $3p$–$4s$ multiplet.

GL collisional excitation to $4p$ levels is quite analogous to the one of $4s$ case. In Figure 4, we present electron excitation cross section for the $3p$ ($^1S_0$)–$4p$ ($^3D_2$) transition in the energy range from threshold to 100 eV as an example. Here also, results from DW and FOMBT are compared with RDW results [17]. More theoretical results [19, 22–24] and also experimental results [20, 25] are presented. We also show Q-C values obtained following Drawin [12] and Sobelman [26]. Experimental results are in rather good agreement with theoretical ones for this transition. Similar evaluations were made for the remaining nine transitions of the $3p$–$4p$ multiplet. It is to be noted that for the $3p$ ($^1S_0$)–$4p$ ($^1S_0$) transition DW and FOMBT calculations give a cross section much higher (more than one order of magnitude) than for all the others. This is not the case with the experimental results, which have been chosen to parametrize this transition. This choice results for the multiplet $3p$–$4p$ to averaged values which are presented afterwards.

Finally, as an example of the $4s$–$4p$ multiplet evaluations we present in Figure 5 the Ar I $4s$ ($^3P_2$)–$4p$ ($^3D_3$) transition case, in the energy range from threshold to 20 eV. In this figure, we compare DW results obtained with three configurations and with eight configurations to Born approximation and RDW [27] results. Available theoretical results [19, 28, 29] are also shown in the figure, only for energies higher than 5 eV. The presented experimental data from two experiments

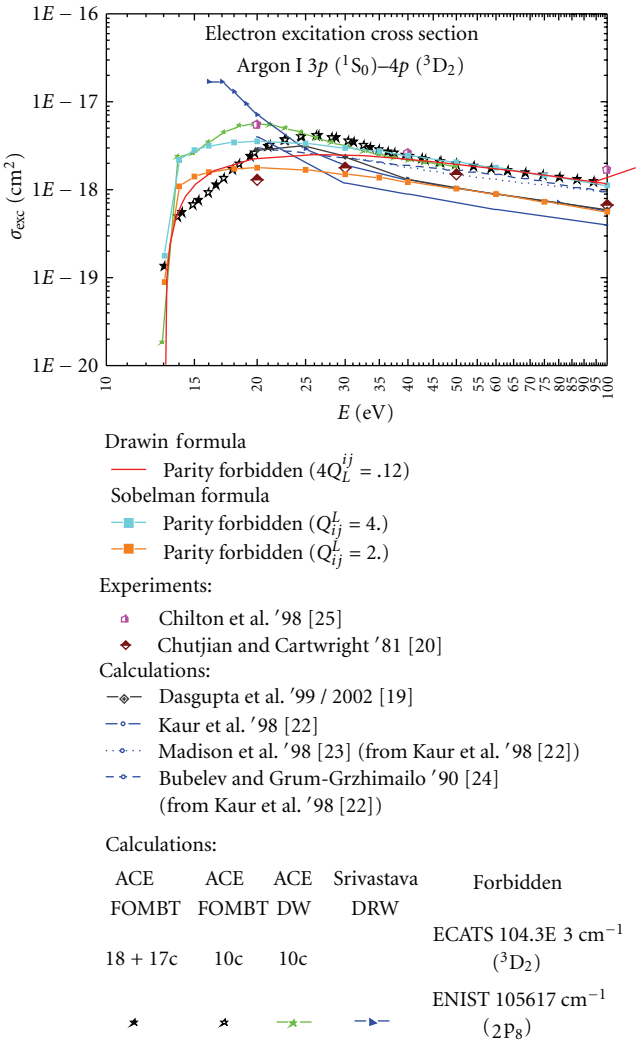

Figure 4: Electron excitation cross section of Ar I $3p\ (^1S_0)$–$4p\ (^3D_2)$.

of Boffard et al. [30, 31] and one of Piech et al. [32] are in rather good agreement with calculations. This is especially the case for the more recent experiment [31] which gives results rather similar to the values obtained when using the Q-C formula with conveniently chosen parameters.

Extended evaluations similar to ones described here succinctly allow for a reliable Ar I data base. They are completed by the well-known calculations of the parameters concerning the inverse processes (Einstein B_{ij} coefficients, see, e.g., the Appendix in Ashida et al. [33], collisional deexcitations, calculated using the principle of detailed balancing, see, e.g., Lieberman and Lichtenberg 2005 [34, page 267], etc.). The global excitation rate curves used in the present work for the GL excitation to the $4s$ and $4p$ levels in case of a Maxwellian distribution are shown in Figures 6 and 7, as obtained by our evaluations. In those figures, averaged results from DW and FOMBT calculations with seven configurations obtained directly from the LANL codes (http://aphysics2.lanl.gov/tempweb/) are also presented. Averaged DW and FOMBT rates are given

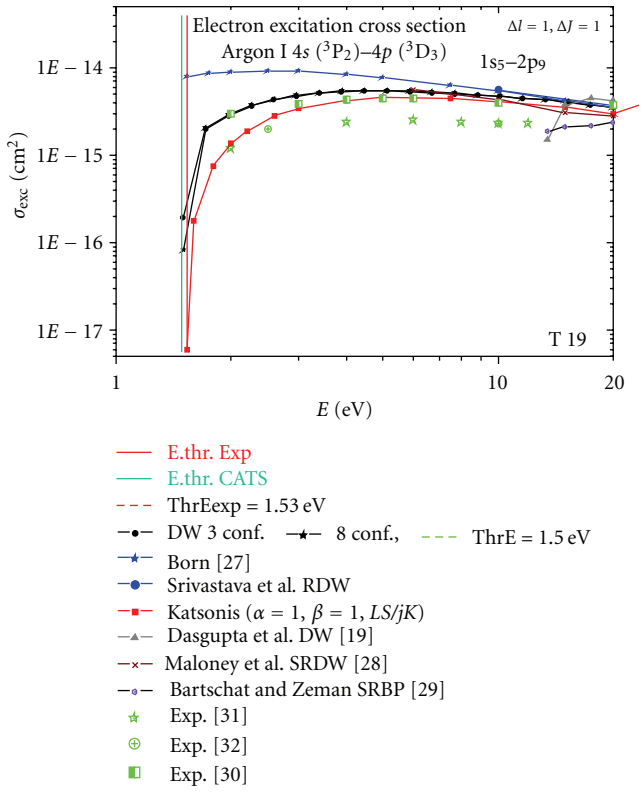

Figure 5: Electron excitation cross section of Ar I $4s\ (^3P_2)$–$4p\ (^3D_3)$.

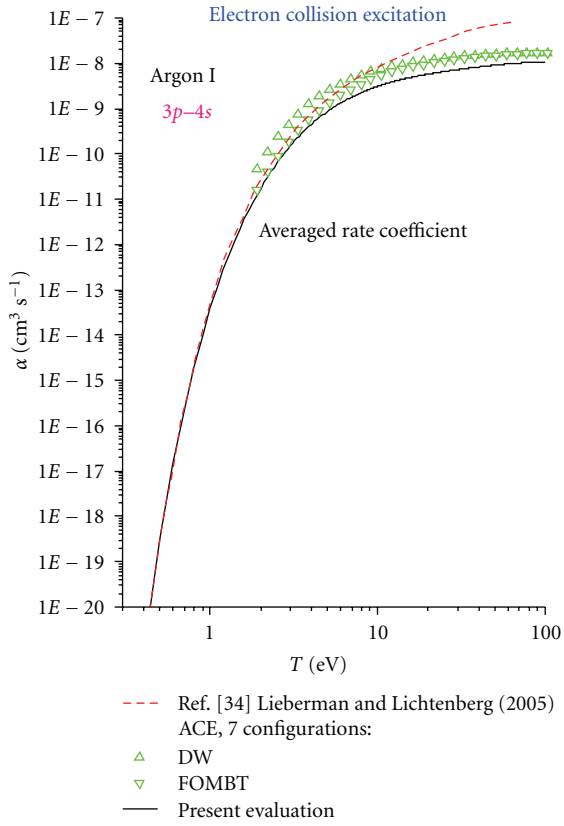

Figure 6: Averaged electron excitation rate coefficient of Ar I $3p$–$4s$ from 0.3 to 100 eV.

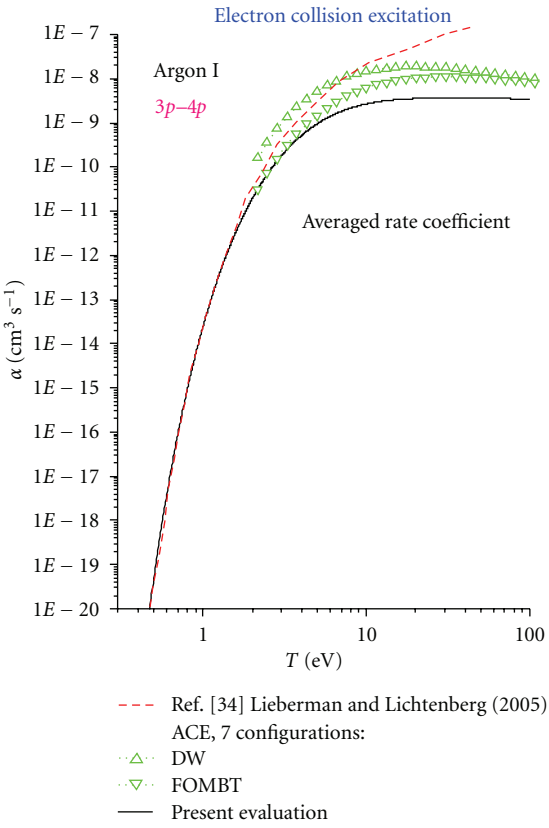

Figure 7: Averaged electron excitation rate coefficient of Ar I $3p$–$4p$ from 0.3 to 100 eV.

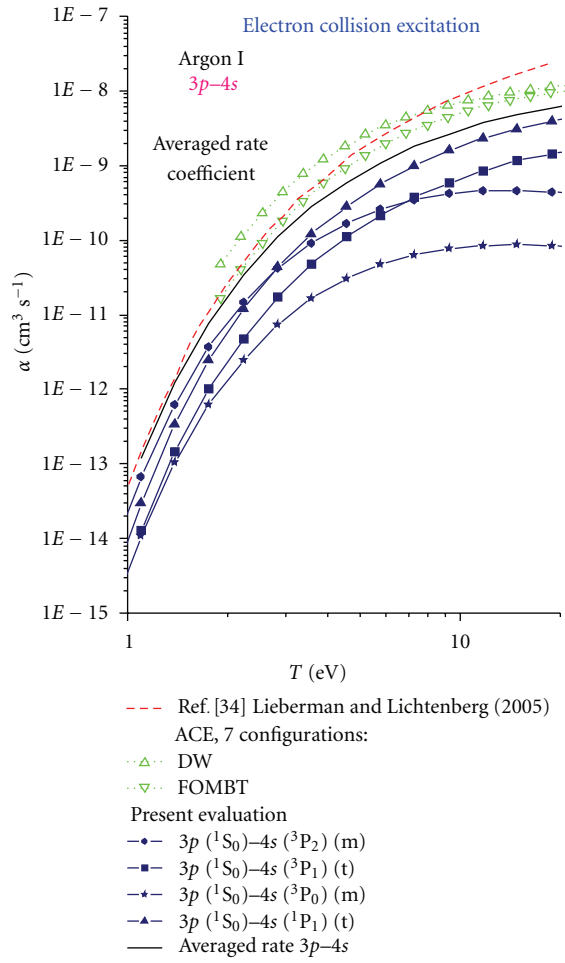

Figure 8: Averaged and individual electron excitation rate coefficients of Ar I $3p$–$4s$ in the energy range from 1 to 20 eV.

from 2 eV temperatures and higher. They are compared with similar values coming from the formulas contained in Table 3.3 from the second edition of the book by Lieberman and Lichtenberg (2005) [34, page 81]. Our results are in a very good agreement with those reported by these authors around 1 eV and lower. This is not the case for higher energies, because the empirical formulas recommended for the excitation values were meant for low-energy evaluations; the empirical formula $A(T_e)^B \exp(-\Delta E/T_e)$ as reported by Kannari et al. [35], based on earlier work [36–39], constitutes a handy approximation valid for the low-energy region, but cannot describe the high-energy part of the rate for a Maxwellian distribution, as important theoretical and experimental work was not available at this time.

In Figure 8, we present in detail the excitation rate coefficients in the region from 1 to 20 eV for the Ar I $3p$–$4s$ transitions and their average. The figure shows our averaged results obtained from the individual cross sections evaluated as in the example of Figure 3. Following a standard procedure, the evaluated cross sections are integrated over a Maxwellian distribution, averaged according to the statistical weights of the lower levels and parametrized. The four individual rate coefficients used for the calculation of the average rate are also shown separately in Figure 8. Here, the average is in fact a sum, because there is only one lower level $3p^5$ in the averaged multiplet. We also plotted in the figure the formula proposed by Kannari et al. [35] and the results obtained from DW and FOMBT calculations. In the low-temperature region ($T_e < 1$ eV), our evaluated results are exactly the same with those coming from the formula. With increasing temperature, an increasing discrepancy is observed.

Comparing the theoretical results obtained by any model using averaged levels with the experimental spectra calls for a separate detailed collisional-radiative (C-R) model of the Ar I. This C-R model is used here to calculate the necessary individual population of each fine structure $4s$, $4p$ level, on the basis of the global $4s$ and $4p$ populations coming from the kinetic model. The calculated spectral line intensities can be compared with the corresponding experimental spectral line intensities and hence allow for the validation of the model.

4. The Arcjet Plasma Source

The studied arcjet is an axisymmetric D.C. plasma source running at reduced pressure. It is schematically shown in Figure 9. A divergent nozzle made of Copper operates as the anode; the cathode is a small flat disk made of W, WTh alloy, or Zr, inserted near a 4 mm diameter cylindrical anode throat

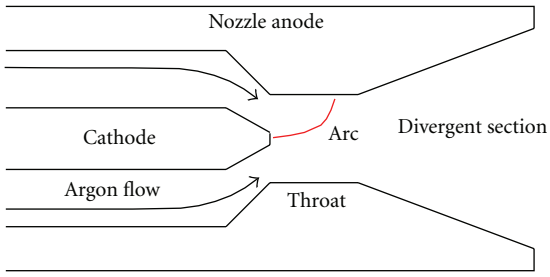

Figure 9: Schematic view of the arcjet.

of 5 mm length. The conical divergent part of the nozzle is 30° in half angle and 55 mm in length. The arc is sustained between the cathode and the anode, each electrode having a separated water cooling circuit, thus allowing a separated evaluation of the energy exchange. The distance between the anode and the cathode is generally around 1 mm, the minimum being strongly dependent on the nature of the used gas. The discharge current is controlled by the arc power supply.

The plasma flow delivered by this arcjet is axisymmetric along the arcjet source axis and stationary, no anode arc foot movement is observed at low pressure. At the exit of the nozzle, the flow is supersonic with a Mach number around 5.

Explicit introduction of the averaged Argon 4*s*, 4*p* excited levels population in the chemical processes constitutes a substantial refinement in the present arcjet modeling. It allows for a detailed monitoring of the arcjet functioning through optical emission spectroscopy on the basis of the "red" Argon I line intensities. Such an improvement has been introduced early [35] in a study of KrF lasers excited by electron beam with Argon buffer gas by means of an advanced kinetic model. More recently, the plasma behavior of a rather high-density plasma reactor with Argon buffer gas was studied [33] using a (global) model containing the four 4*s* and the ten 4*p* levels of the neutral Argon atom. The importance of these studies was illustrated in Lieberman and Lichtenberg (2005) [34]. The present work introduces a consideration of the Ar I excited states in a previous arcjet modeling [40].

5. Ar(4*s*) and Ar(4*p*) Populations with a Low-Plasma Coupling

In order to determine local parameters such as static pressure, electron and heavy species temperatures, plasma density, and plasma velocity computation of the hydrodynamic parameters of the plasma flow in the arcjet have been performed using a fluid description under several assumptions. The plasma flow is assumed to be stationary; therefore, no arc foot movement is introduced on the anode surface. Vortex flow movements due to the injection device are neglected due to the axial pressure gradient and also turbulence effects because of the small values of the local Reynolds number. Moreover, the erosion rate of the cathode is weak enough to be negligible, the flow is supposed to be two-dimensional (r, z), and azimuthal rotation of the arc is not taken into account. The flow can be represented as being of continuous-fluid type and is described by the Navier-Stokes equations without slip-wall conditions. It is assumed that the ionization involves formation of only singly charged Argon ions and that the plasma is locally characterized by two kinetic temperatures namely electron temperature T_e and temperature T of ions and neutral atoms, collectively named heavy particles. The arcjet is divided into two zones: the electric arc zone corresponding to the throat of the nozzle and the expanded plasma jet located in the divergent part of the arcjet. In this approach, the local and the axial electric field are a function of the coordinates r and z and a mean value can be calculated as

$$\langle E(z)\rangle = \frac{I}{2\pi \int_0^{r_c} \sigma r dr}, \tag{1}$$

where σ is the electric conductivity expressed according to Devoto [41] with the average electron-neutral collision cross section taken from [42], and r_c is the throat radius. The arc current I is introduced as an input which is kept constant along the throat of the nozzle. The local plasma velocity, mass density, and mass and momentum balance equations are written in cylindrical coordinate system formulated by Chang and Pfender [43] and Beulens et al. [44] as follows:

$$\begin{aligned}
&\frac{\partial}{\partial z}(\rho u) + \frac{1}{r}\frac{\partial}{\partial r}(r\rho v) = 0,\\
&\frac{\partial}{\partial z}(\rho u^2) + \frac{1}{r}\frac{\partial}{\partial r}(r\rho uv) = \frac{1}{r}\frac{\partial}{\partial r}\left(r\mu\frac{\partial u}{\partial r}\right) - \frac{\partial p}{\partial z},\\
&\frac{\partial}{\partial z}(\rho uv) + \frac{1}{r}\frac{\partial}{\partial r}(r\rho v^2) = \frac{2}{r}\frac{\partial}{\partial r}\left(r\mu\frac{\partial v}{\partial r}\right) - \frac{2\mu v}{r^2} - \frac{\partial p}{\partial r},
\end{aligned} \tag{2}$$

where u and v are the axial and radial velocity components, respectively, ρ the global mass density, μ the gas viscosity, and p the pressure. The mass density and pressure are related to particles densities and temperatures by the Dalton's law. According to the level of pressure in the nozzle, no-slip-wall conditions for velocity and temperature are introduced. For singly ionized Argon plasma in quasineutrality condition, only one electron continuity equation is needed for the plasma balance composition:

$$\frac{\partial}{\partial z}(n_e u) + \frac{1}{r}\frac{\partial}{\partial r}(r n_e v) = \frac{1}{r}\frac{\partial}{\partial r}\left(r D_a \frac{\partial n_e}{\partial r}\right) + S_e, \tag{3}$$

where n_e is the electron density, S_e the electron source, and D_a the electron ambipolar diffusion coefficient [45].

The electron density n_e (equals to the ion density n_+) plays a basic role in the plasma chemistry. The electron energy balance equation, expressed in terms of temperature instead of energy, is

$$\begin{aligned}
&\frac{5}{2}n_e k\left(u\frac{\partial T_e}{\partial z} + v\frac{\partial T_e}{\partial r}\right)\\
&\quad = \frac{1}{r}\frac{\partial}{\partial r}\left(r\kappa_e\frac{\partial T_e}{\partial r}\right) + u\frac{\partial}{\partial z}(n_e k T_e) + v\frac{\partial}{\partial r}(n_e k T_e)\\
&\qquad + \frac{j^2}{\sigma} - Q_{\text{elas}} - Q_{\text{rad}} - S_e E_{\text{ion}},
\end{aligned} \tag{4}$$

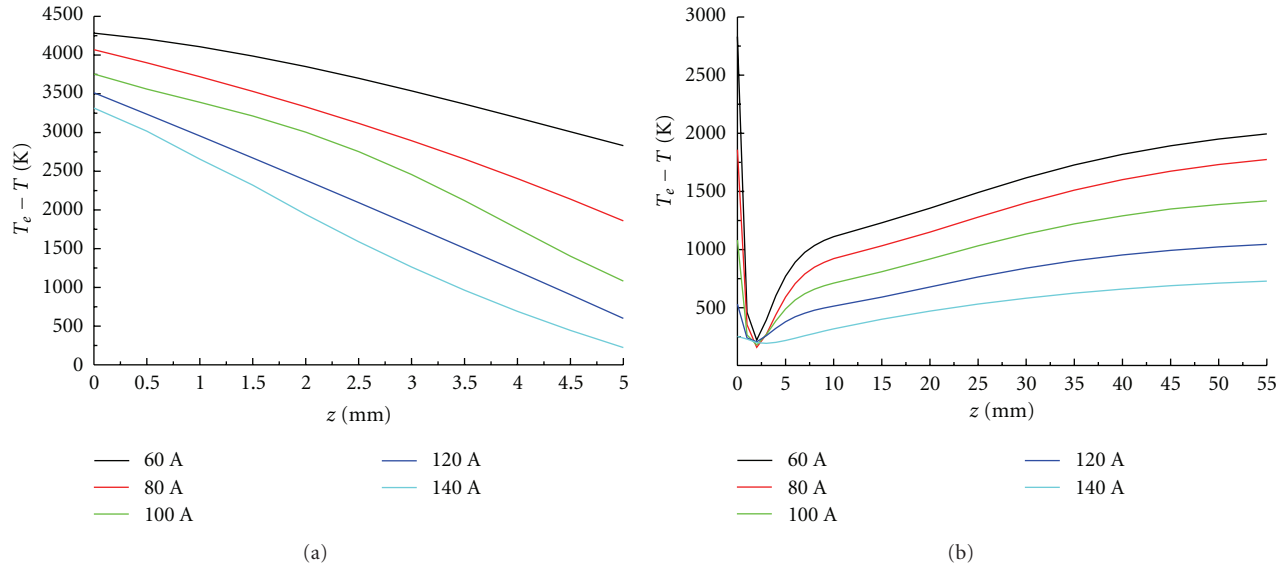

Figure 10: Differences between electron T_e and heavy particles T temperatures: (a) along the throat axis, (b) along the divergent part axis. Only single-ground states for Ar I and Ar II are considered.

with k for the Boltzmann constant; κ_e is the electron thermal conductivity given by Devoto [45]. j^2/σ is the heat input by Joule effect, where j stands for the current density, and E_{ion} is the atom ionization energy. Q_{rad} represents the radiation loss [46] while Q_{elas} is the energy exchange between electrons and heavy particles in elastic collisions [43]. The latter can be expressed as $Q_{\text{elas}} = B(T - T_e)$. In the second and third terms of the above equation right hand side, $n_e k T_e$ can be replaced by p_e, the electron pressure.

The energy balance of the heavy particles is written as

$$\frac{5}{2} n_h k \left(u \frac{\partial T}{\partial z} + v \frac{\partial T}{\partial r} \right) = \frac{1}{r} \frac{\partial}{\partial r} \left(r \kappa_h \frac{\partial T}{\partial r} \right) + u \frac{\partial p_h}{\partial z} + v \frac{\partial p_h}{\partial r} + Q_{\text{elas}}, \quad (5)$$

where κ_h is the heavy particles thermal conductivity and p_h is the heavy particles pressure. As presented, the balance equations are directly related to temperatures (T_e, T) instead of energies $(\varepsilon_e, \varepsilon_T)$.

Balance equations have been numerically solved to calculate plasma density, gas concentrations, pressure, temperatures (T_e, T), and velocity of the plasma flow, using the numerical code developed at IEPE. Electron density and concentration of neutral Ar and its single ion only in ground state are introduced in this stage. The obtained differences between the temperatures (T_e, T) along the plasma axis in the throat and in the divergent part of the nozzle are presented in Figure 10, where only single-ground states Ar, Ar^+ are considered. In a second step, the populations of the Argon states Ar(4s) and Ar(4p) have been calculated by using the profiles of hydrodynamic parameters obtained with the fluid code Papyrus.

As was explained previously, the Ar(4s) configuration is formed in four levels, two metastable and two transitory. In a first approximation, they are assembled in a sole level for which a collective reaction rate was evaluated as a weighted average of the separate transitions of the multiplet, evaluated by Katsonis and Berenguer [10, 11]. The same approach was used for the Ar(4p) configuration, consisting of ten levels.

Population of the neutral Argon configuration Ar(4s) is due to the electron collision excitation processes from the Ar I GL ($3p^6$, neutral ground level) and de-excitation from Ar(4p) and from Ar II GL (ion ground level) recombination. The 4s electron excitation rate has been calculated as a function of the electron temperature, up to 100 eV. The corresponding de-excitation rate has been calculated through the detailed balance principle as a function of the electron temperature. The probability of transition for radiative de-excitation of Ar(4p) to Ar(4s) and to Ar I GL has also been evaluated. Ionization from Ar(4s) and Ar(4p) and collisional recombination from Ar II GL are also introduced.

For Ar(4p), processes taken into account are electron collision excitation from the Ar I GL ($3p^6$, ground level of the neutral atom) and from Ar(4s) and electron recombination from Ar II GL (ion ground state). The rates of electron excitation have also been calculated for each of the ten Ar I 4p levels and then a global rate has been approximated as a function of the electron temperature, also up to 100 eV.

The balance equations for the populations of Ar(4s) and Ar(4p) are

$$\begin{aligned} \frac{d\text{Ar}(4s)}{dt} &= k_1(T_e)\ \text{Ar}(3p) n_e - k_4(T_e)\text{Ar}(4s) n_e \\ &\quad - k_3(T_e)\text{Ar}(4s) n_e + k_6(T_e)\text{Ar}(4p) n_e \\ &\quad - k_8(T_e)\text{Ar}(4s) n_e + R_{4s}(T_e) n_+ n_e \\ &\quad - A_{ij}(1)\text{Ar}(4s) + A_{ij}(1)\text{Ar}(3p) \\ &\quad - A_{ij}(2)\text{Ar}(4s) + A_{ij}(2)\text{Ar}(4p), \end{aligned}$$

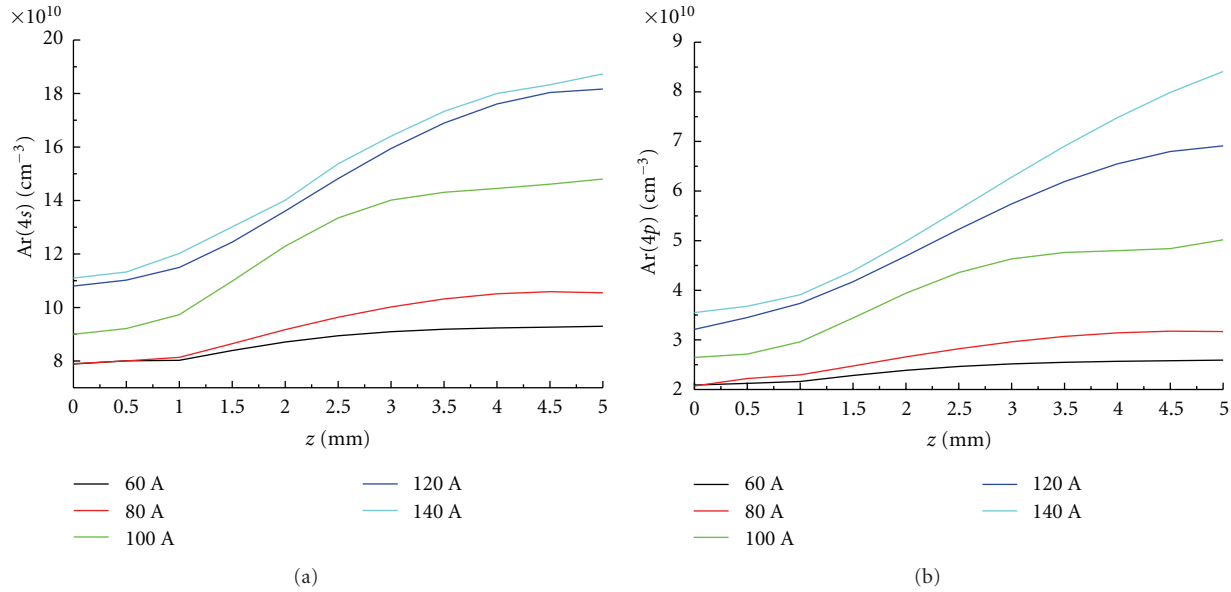

Figure 11: Populations along the throat axis of: (a) Ar(4s), (b) Ar(4p).

$$\frac{d\mathrm{Ar}(4p)}{dt} = k_2(T_e)\mathrm{Ar}(3p)n_e + k_3(T_e)\mathrm{Ar}(4s)n_e - k_5(T_e)\mathrm{Ar}(4p)n_e - k_6(T_e)\mathrm{Ar}(4p)n_e - k_9(T_e)\mathrm{Ar}(4p)n_e + R_{4p}(T_e)n_+n_e + A_{ij}(2)\mathrm{Ar}(4s) - A_{ij}(2)\mathrm{Ar}(4p). \quad (6)$$

In these equations, k_i are the specific rates of each excitation or ionization process, R_{nl} are the radiative recombination rates towards the nl configuration, $A_{ij}(1/2)$ are distinct transition probabilities for the corresponding transition in parenthesis, and Ar(3p/4p/4s) are the corresponding populations. Obviously, in our case, $n_+ = n_e$. The above equations are solved at each point along the axis of the nozzle in the throat and in the divergent part in steady state approximation and by using the values of T_e, the neutral Ar population (Ar I), and the Ar ion population (Ar^+)—the last being equal to e^- according to the plasma neutrality assumption as previously noted—as calculated by the Navier-Stokes type code from IEPE.

Figures 11 and 12 present the evolution of the populations of Ar(4s) and Ar(4p) for a discharge current in the range 60 A to 140 A along the throat axis and the divergent axis. These two populations are increasing in the throat due to the input arc energy; they decrease in the divergent part. On the whole, they increase with the arc power, the population of Ar(4s) being greater than the Ar(4p) one.

In order to examine the relative contributions of the processes involving a change in the populations of the two states Ar(4s) and Ar(4p), the production rates of the different contributions rather than the specific rates have been calculated in the throat axis and in the nozzle divergent part using the values of concentrations obtained by the numerical simulations. Initially, we compared the production rates obtained with a nominal arc current of 60 A.

The rates obtained for the Ar(4s) populations are quite constant along the throat axis as shown on Figure 13. This is mainly due to the slight variation of the electron temperature along the throat, between 11200 K and 11695 K and of the electron density similarly, between $2.05 \cdot 10^{16}\,\mathrm{cm}^{-3}$ and $2.61 \cdot 10^{16}\,\mathrm{cm}^{-3}$. However, the different processes do not have the same importance. The main processes considered are summarized in Table 3. In order to get an idea of their relative importance, indicative values pertaining to the restricted temperature range observed in the throat are also included in Table 3.

Three collisional processes are dominant and population-depopulation are globally quite equivalent:

(i) depopulation of 4s due to excitation towards 4p, by $\mathrm{Ar}(4s) + e^- \Rightarrow \mathrm{Ar}(4p) + e^-$, production rate = $-(4 \div 5) \cdot 10^{20}\,\mathrm{cm}^{-3}\,\mathrm{s}^{-1}$ (specific rate k_3),

(ii) population of 4s from the GL by $\mathrm{Ar}(3p) + e^- \Rightarrow \mathrm{Ar}(4s) + e^-$ (specific rates k_1),

(iii) population of 4s from 4p $\mathrm{Ar}(4p) + e^- \Rightarrow \mathrm{Ar}(4s) + e^-$ with production rates around $+(2 \div 3) \cdot 10^{20}\,\mathrm{cm}^{-3}\,\mathrm{s}^{-1}$ (specific rates k_6).

The next collisional effect in decreasing order of importance, is the depopulation of the state Ar(4s) leading to population of the Ar ground state by electron collisions, that is, $\mathrm{Ar}(4s) + e^- \Rightarrow \mathrm{Ar}(3p) + e^-$, with a production rate of $-1 \cdot 10^{18}\,\mathrm{cm}^{-3}\,\mathrm{s}^{-1}$ (specific rate k_4). For the Ar^+ ground level, the main radiative process is its radiative recombination to Ar(4s) according to $\mathrm{Ar}^+ + e^- \Rightarrow \mathrm{Ar}(4s) + h\nu$, with production rate $+10^{19}\,\mathrm{cm}^{-3}\,\mathrm{s}^{-1}$ (R_{4s}), followed by recombination to 4p. The radiative effects between Ar(4s) and Ar(3p), Ar(4s)

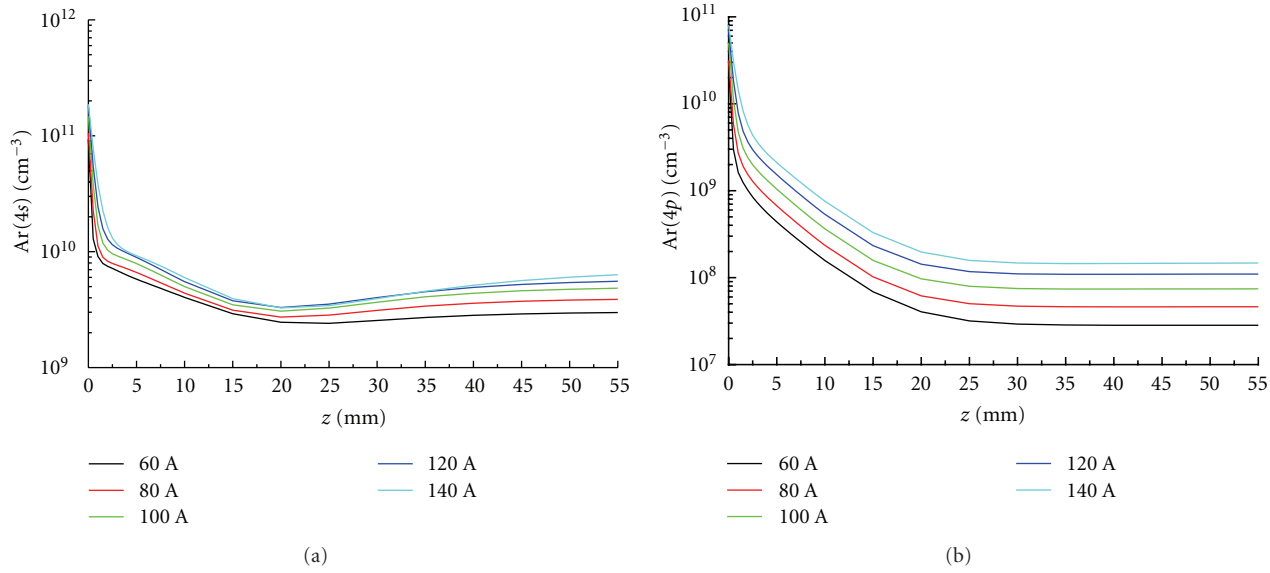

Figure 12: Populations along the divergent part axis of: Ar(4s), Ar(4p).

and Ar(4p), with rates of the order of $-10^{10}\,\mathrm{cm}^{-3}\,\mathrm{s}^{-1}$ and $-10^{5}\,\mathrm{cm}^{-3}\,\mathrm{s}^{-1}$ have been neglected.

In the nozzle divergent part (Figure 14), the production rates due to electronic collisions are decreasing strongly, mainly in the first 2 mm from the throat exit for the depopulation by $\mathrm{Ar}(4s) + \mathrm{e}^- \Rightarrow \mathrm{Ar}(3p) + \mathrm{e}^-$ (specific rate k_4); this effect becomes dominant after 10 mm. As shown on Figure 14, the three next rates have similar behaviors and amplitudes. Finally, the $3p \rightarrow 4s$ excitation rate is strongly decreasing along the axis. After a distance of 35 mm, all the production rates are quite constant up to the nozzle divergent part exit.

We address now the 4p case, the main production rates are all constant along the throat axis. The main process (Figure 13) is the population from the Ar ground state by $\mathrm{Ar}(3p) + \mathrm{e}^- \Rightarrow \mathrm{Ar}(4p) + \mathrm{e}^-$ (k_2) with a production rate around $+10^{20}\,\mathrm{cm}^{-3}\,\mathrm{s}^{-1}$. A second important effect is the population from Ar^+ through recombination: $\mathrm{Ar}^+ + \mathrm{e}^- \Rightarrow \mathrm{Ar}(4p) + h\nu$ (R_{4p}) for which the production rate is around $+2 \cdot 10^{19}\,\mathrm{cm}^{-3}\,\mathrm{s}^{-1}$. The rate of depopulation from $\mathrm{Ar}(4p) + \mathrm{e}^- \Rightarrow \mathrm{Ar}(4s) + \mathrm{e}^-$ (k_8) is between $-6 \cdot 10^{18}\,\mathrm{cm}^{-3}\,\mathrm{s}^{-1}$ and $-10^{19}\,\mathrm{cm}^{-3}\,\mathrm{s}^{-1}$; the rate of depopulation of Ar(4s) through excitation to Ar(4p): $\mathrm{Ar}(4s) + \mathrm{e}^- \Rightarrow \mathrm{Ar}(4p) + \mathrm{e}^-$ (k_5) is around $2 \cdot 10^{17}\,\mathrm{cm}^{-3}\,\mathrm{s}^{-1}$.

In the divergent part of the nozzle (Figure 14), all the production rates are decreasing up to 35 mm, after which they become quite constant. Especially the GL excitation to 4p, the production rate decreases several orders of magnitude.

6. Conclusions

Using detailed evaluations of the transitions probabilities and of the excitation cross sections for the lower Ar* levels, we obtained a set of global rates for the averaged configurations 4s and 4p. This set is valid in a very large energy region; hence, it can be used in a large number of applications. Here, it is used in arcjet modeling as a typical application. Velocities and temperatures of the species present in the arcjet have been previously calculated in the arcjet together with pressure and density, using a Navier-Stokes type code [40]. In so doing, dissipative effects and arc-gas exchanges have been taken into account for different reentry problems (CO_2–N_2, N_2–CH_4, air). We hereby significantly extend this work, applying a version of the code papyrus in Argon plasma behavior calculations. They concern an Ar-fed arcjet in which, besides the main constituents Ar, Ar^+ and e^-, Ar* species excited in two collective levels corresponding to

Table 3: Main processes and their coefficients.

Processes	k_i/R_{nl}	Process type
$\mathrm{Ar}(3p) + \mathrm{e}^- \Rightarrow \mathrm{Ar}(4s) + \mathrm{e}^-$	k_1	Exc
$\mathrm{Ar}(3p) + \mathrm{e}^- \Rightarrow \mathrm{Ar}(4p) + \mathrm{e}^-$	k_2	Exc
$\mathrm{Ar}(4s) + \mathrm{e}^- \Rightarrow \mathrm{Ar}(4p) + \mathrm{e}^-$	k_3	Exc
$\mathrm{Ar}(4s) + \mathrm{e}^- \Rightarrow \mathrm{Ar}(3p) + \mathrm{e}^-$	k_4	De-exc
$\mathrm{Ar}(4p) + \mathrm{e}^- \Rightarrow \mathrm{Ar}(3p) + \mathrm{e}^-$	k_5	De-exc
$\mathrm{Ar}(4p) + \mathrm{e}^- \Rightarrow \mathrm{Ar}(4s) + \mathrm{e}^-$	k_6	De-exc
$\mathrm{Ar}(3p) + \mathrm{e}^- \Rightarrow \mathrm{Ar}^+ + 2\mathrm{e}^-$	k_7	Ion
$\mathrm{Ar}(4s) + \mathrm{e}^- \Rightarrow \mathrm{Ar}^+ + 2\mathrm{e}^-$	k_8	Ion
$\mathrm{Ar}(4p) + \mathrm{e}^- \Rightarrow \mathrm{Ar}^+ + 2\mathrm{e}^-$	k_9	Ion
$\mathrm{Ar}^+ + \mathrm{e}^- \Rightarrow \mathrm{Ar}(3p) + \mathrm{h}\nu$	R_{3p}	RR
$\mathrm{Ar}^+ + \mathrm{e}^- \Rightarrow \mathrm{Ar}(4s) + \mathrm{h}\nu$	R_{4s}	RR
$\mathrm{Ar}^+ + \mathrm{e}^- \Rightarrow \mathrm{Ar}(4p) + \mathrm{h}\nu$	R_{4p}	RR

Exc: electron collision excitation.
De-exc: electron collision de-excitation.
Ion: ionization.
RR: radiative recombination.

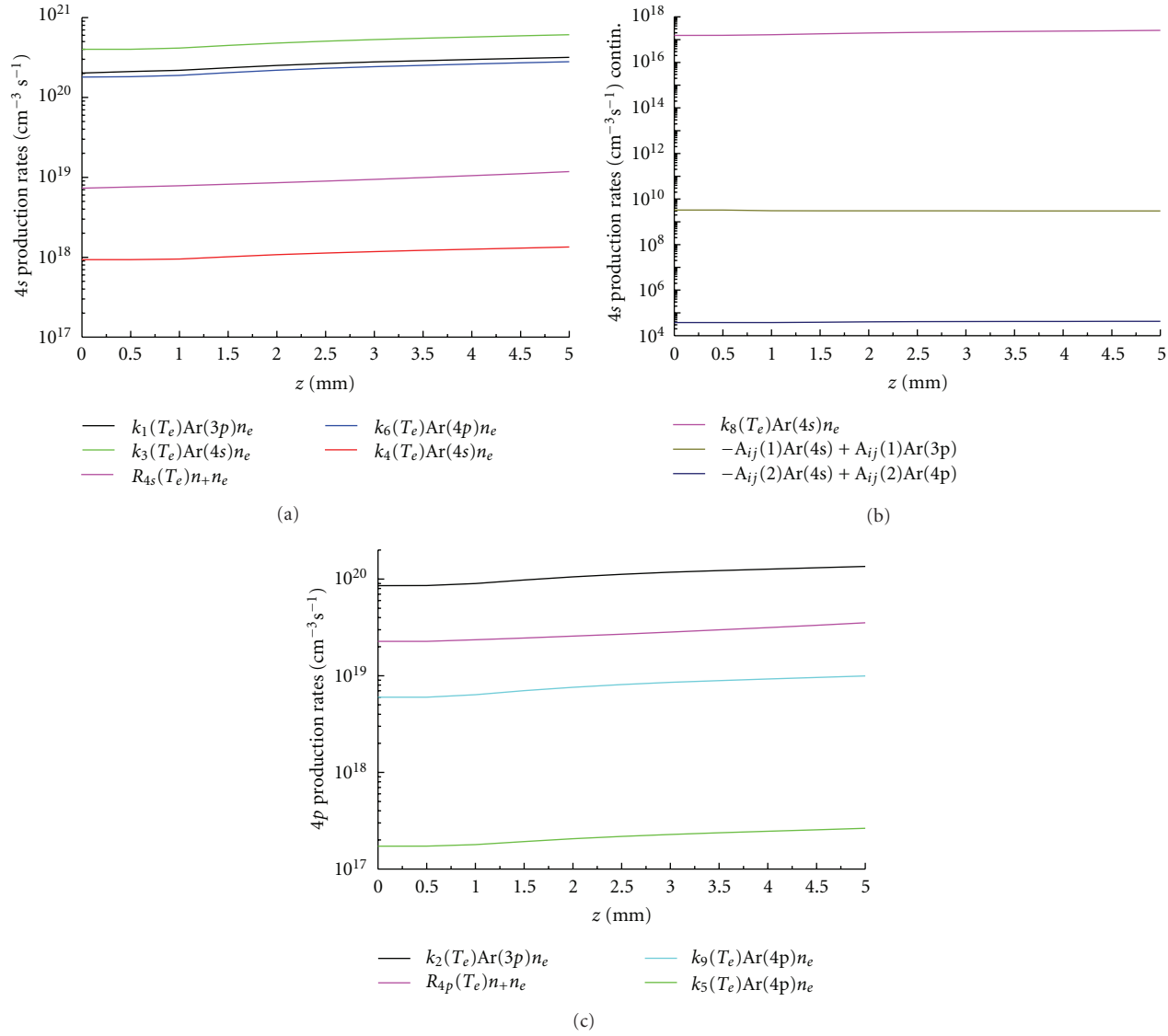

FIGURE 13: Production rates of Ar(4s) and Ar(4p) along the throat axis for $I = 60$ A.

the Ar(4s) and Ar(4p) configurations have been considered. Separate introduction of the two species in the fluid code allows for approximate evaluation of the Ar(4s) and Ar(4p) global levels populations. The obtained evolution is found consistent with the expected collective behavior of the plasma, according to results coming from the used code. Whenever the calculation time allows, separate consideration of the transitory levels and of the metastable part of the 4s and of the quasimetastable part of the 4p configurations will be taken into account.

It is important that the excited level populations obtained now allow for a direct and detailed optical diagnosis of the experiment in various points inside the arcjet. This is a prerequisite for a validation of codes used for the plasma study and more specifically lead to the populations evaluation. A study of the experimentally evaluated populations in arcjet is under way, in conjunction with application of a detailed collisional-radiative model [47].

Nomenclature

A_{ij}:	Transition probability, level j to i
$A_{ij}(1/2)$:	Transition probability for transition of 4s/4p
Ar I, II, ...:	Successive spectra of the argon homonuclear sequence
Ar^+:	One time ionized argon, Ar II (GL)
Ar^*:	Excited Ar I
B_{ij}:	Einstein coefficient
E_{ion}:	Ionization energy of Ar I atom
I:	Arc current
j:	Current density
j_c:	Total angular momentum of the core
jK/LS:	Coupling schemes
k:	Boltzmann constant
k_i:	Specific rate coefficient for a transition i
l:	Orbital quantum number, $s = 0$, $p = 1$, $d = 2$, $f = 3$, ...

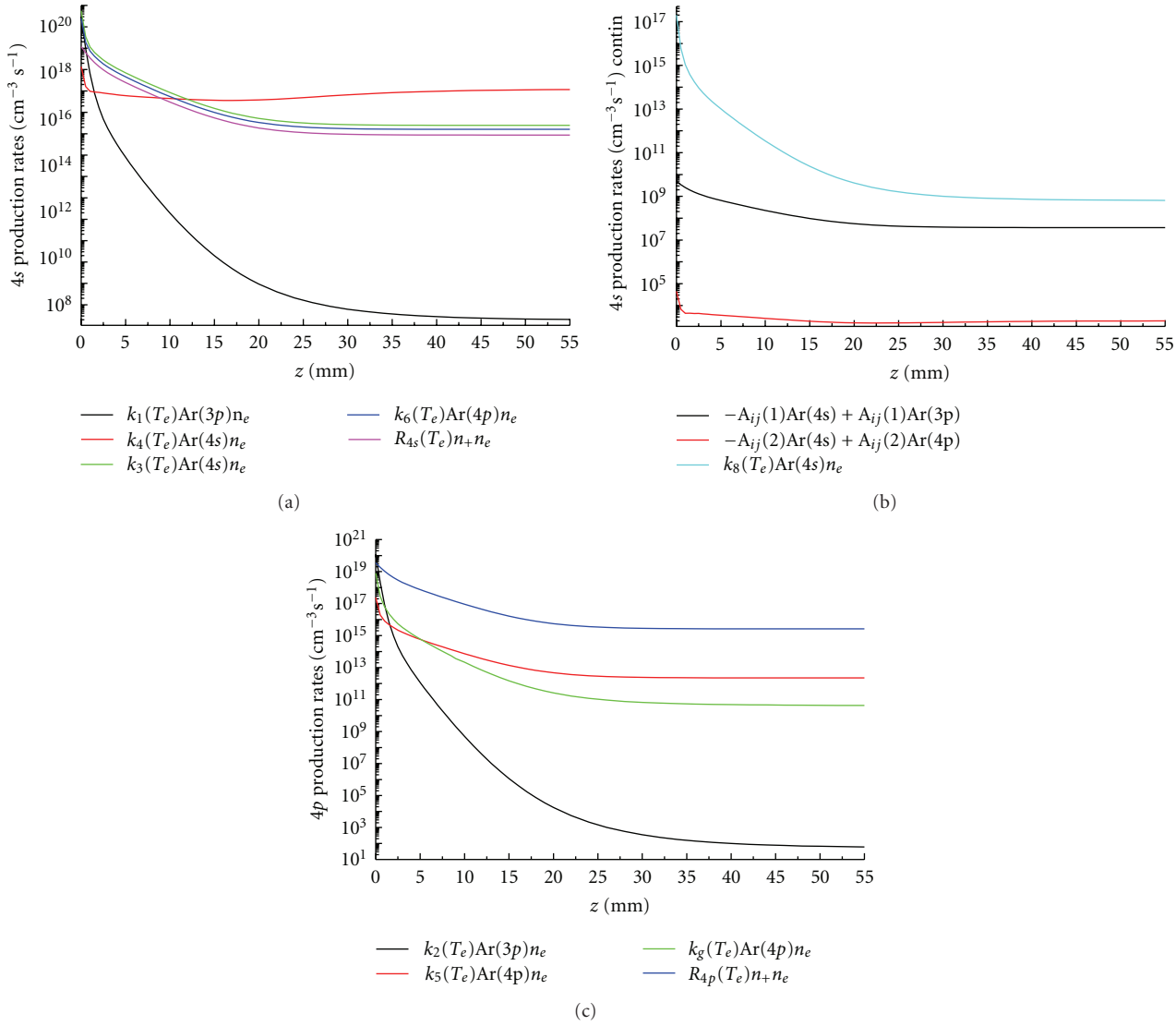

Figure 14: Production rates of Ar(4s) and Ar(4p) along the divergent part axis for $I = 60$ A.

m: Metastable (level)
n: Principal quantum number, here $n = 3, 4$
n_e: Electronic density
n_+: Ion density
p: Pressure
p_e: Electron pressure
p_h: Heavy particles pressure
q-m: Quasimetastable (level)
Q_{rad}: Radiation loss
Q_{elas}: Energy exchange between electrons and heavy particles in elastic collisions
R_{nl}: Radiative recombination rates towards the nl configuration
r_c: Throat radius
S_e: Electron source
t: Transitory (level)
T: Kinetic temperature
T_e: Electronic temperature
T_{vj}: Vibrational temperature
T_{rj}: Rotational temperature
α: Rate coefficient
ε_e, ε_T: Electronic and kinetic energies
u, v: Axial and radial velocity components
κ_e: Electron thermal conductivity
κ_h: Heavy particles thermal conductivity
μ: Gas viscosity
ν_a: Electron ambipolar diffusion coefficient
ρ: Global mass density
σ: Electric conductivity
σ_{exc}: Electron collision excitation cross section
σ_{I}: Electron collision ionization cross section.

Acronyms

ACE: Atomic collisions with electrons code
CATS: Cowan atomic structure code
CbA: Coulomb approximation code

C-R: Collisional-radiative
CTMC: Classical trajectory Monte Carlo
D.C.: Direct current
DEDALOS: Data evaluation and diagnostics algorithms of systems
DW: Distorted wave approximation
FOMBT: First order many body theory
GL: Ground level compound, composed by one sole level for Ar I and two for Ar II
ICP: Inductively coupled plasma
IEPE: Institute of Electric Power Engineering
LANL: Los Alamos National Laboratory
NIST: National Institute of Standards and Technology, Gaithersburg (USA)
Q-C: Quasiclassical
RDW: Relativistic distorted wave approximation
TPS: Thermal protection system
UV: Ultraviolet spectral region.

Acknowledgments

The authors thank the unknown reviewers for their comments which contributed to the present improved form of the paper.

References

[1] K. Katsonis and H. W. Drawin, "Transition probabilities for argon(I)," *Journal of Quantitative Spectroscopy and Radiative Transfer*, vol. 23, no. 1, pp. 1–55, 1980.

[2] K. Katsonis, C. Berenguer, and M. Cornille, "Atomic data in Ar thruster multidimensional modeling and optical diagnostics," in *Proceedings of the 31st International Electric Propulsion Conference, (IEPC '09)*, Ann Arbor, Mich, USA, September 2009.

[3] K. Katsonis, C. Berenguer, and M. Cornille, "Ar I transition probabilities and excitation cross sections involving the 4s metastable levels and the 4/5p configurations," Report LPGP-GA-22, Orsay, France, 2008.

[4] K. Katsonis, C. Berenguer, R. Srivastava et al., "Ar I transition probabilities and excitation cross sections involving the 4s metastable levels and the 4/5p configurations," in *Proceedings of the 40th European Group for Atomic Systems Conference, (EGAS '08)*, Graz, Austria, July 2008.

[5] D. R. Bates and A. Damgaard, "The calculation of the absolute strengths of spectral lines," *Philosophical Transactions of the Royal Society of London. Series A*, vol. 242, no. 842, pp. 101–122, 1949.

[6] W. Eissner, M. Jones, and H. Nussbaumer, "Techniques for the calculation of atomic structures and radiative data including relativistic corrections," *Computer Physics Communications*, vol. 8, no. 4, pp. 270–306, 1974.

[7] J. Abdallah Jr., R. E. H. Clark, and R. D. Cowan, "CATS: the Cowan Atomic Structure Code," Report LA-11436-M, Vol I, 1988.

[8] C. Berenguer, K. Katsonis, S. Danakas, S. Cohen, P. Tsekeris, and M. Cornille, "Study of the first three Ar I, II, III spectra using a C-R model," in *Proceedings of the 6th International Conference on Atomic and Molecular Data and Their Applications, (ICAMDATA '08)*, Beijing, China, October 2008.

[9] H. M. Grosswhite and G. H. Diecke, "Important atomic spectra," in *American Institute of Physics Handbook*, D. E. Gray, Ed., pp. 7–58, McGraw-Hill, New York, NY, USA, 1957.

[10] K. Katsonis and C. Berenguer, "Electron collision excitation of the lower Ar I levels," Report LPGP-GA-23, Orsay, France, 2008.

[11] K. Katsonis and C. Berenguer, "Ar I transition probabilities and excitation cross sections from the 4s transitory levels to the 4/5p configurations," Report LPGP-GA-26, Orsay, France, 2009.

[12] H. W. Drawin, "Collision and transport cross sections," Report EURATOM-CEA-FC 383, Fontenay-aux-Roses, France, 1966-1967.

[13] M. Gryziński, "Classical theory of electronic and ionic inelastic collisions," *Physical Review*, vol. 115, no. 2, pp. 374–383, 1959.

[14] K. Katsonis and H. Varvoglis, "The CTMC method as part of the study of classical chaotic hamiltonian systems," *Journal of Physics B*, vol. 28, no. 15, p. L483, 1995.

[15] K. Katsonis, K. Dimitriou, and F. Sattin, "Using three-, four- and five-body CTMC methods in evaluating cross sections in atomic collisions," in *Proceedings of the 3rd International Conference on Atomic and Molecular Data and Their Applications, (ICAMDATA '02)*, Gatlinburg, Tenn, USA, April 2002.

[16] F. Sattin and K. Katsonis, "Electron impact ionization close to the threshold: classical calculations," *Journal of Physics B*, vol. 36, no. 3, pp. L63–L68, 2003.

[17] R. K. Gangwar, K. Katsonis, C. Berenguer et al., "Electron collision excitation of the lower Ar I levels," in *Proceedings of the DAE-BRNS symposium*, pp. 108–109, New Delhi, India, Febraury 2009.

[18] N. T. Padial, G. D. Meneses, F. J. da Paix, G. Csanak, and D. C. Cartwright, "Electron-impact excitation of the lowest four excited states of argon," *Physical Review A*, vol. 23, no. 5, pp. 2194–2212, 1981.

[19] A. Dasgupta, M. Blaha, and J. L. Giuliani, "Electron-impact excitation from the ground and the metastable levels of Ar I," *Physical Review A*, vol. 61, no. 1, Article ID 012703, 10 pages, 1999, Erratum: *Physical Review A*, vol. 65, no. 3, Article ID 039905, 1 page, 2002.

[20] A. Chutjian and D. C. Cartwright, "Electron-impact excitation of electronic states in argon at incident energies between 16 and 100 eV," *Physical Review A*, vol. 23, no. 5, pp. 2178–2193, 1981.

[21] S. Tsurubuchi, T. Miyazaki, and K. Motohashi, "Electron-impact emission cross sections of Ar," *Journal of Physics B*, vol. 29, no. 9, pp. 1785–1801, 1996.

[22] S. Kaur, R. Srivastava, R. P. McEachran, and A. D. Stauffer, "Electron impact excitation of the $np^5(nfl)p$ States of Ar($n = 3$), Kr($n = 4$) and Xe($n = 5$) atoms," *Journal of Physics B*, vol. 31, no. 21, pp. 4833–4852, 1998.

[23] D. H. Madison, C. M. Maloney, and J. B. Wang, "Integral and differential cross section for electron-impact excitation of 12 of the lowest states of argon," *Journal of Physics B*, vol. 31, no. 4, pp. 873–893, 1998.

[24] V. E. Bubelev and A. N. Grum-Grzhimailo, "Excitation of the 2p levels of inert gases by electrons in the distorted-wave approximation: neon and argon," *Optics and Spectroscopy*, vol. 69, no. 2, pp. 178–182, 1990.

[25] J. E. Chilton, J. B. Boffard, R. S. Schappe, and C. C. Lin, "Measurement of electron-impact excitation into the $3p^54p$ levels of argon using Fourier-transform spectroscopy," *Physical Review A*, vol. 57, no. 1, pp. 267–277, 1998.

[26] I. I. Sobelman, *Introduction to the Theory of the Atomic Spectra*, Pergamon Press, Oxford, UK, 1972.

[27] R. Srivastava, A. D. Stauffer, and L. Sharma, "Excitation of the metastable states of the noble gases," *Physical Review A*, vol. 74, no. 1, Article ID 012715, 2006.

[28] C. M. Maloney, J. L. Peacher, K. Bartschat, and D. H. Madison, "Excitation of Ar $3p^5 4s$—$3p^5 4p$ transitions by electron impact," *Physical Review A*, vol. 61, no. 2, Article ID 022701, 5 pages, 2000.

[29] K. Bartschat and V. Zeman, "Electron-impact excitation from the $(3p^5 4s)$ metastable states of argon," *Physical Review A*, vol. 59, no. 4, pp. R2552–R2554, 1999.

[30] J. B. Boffard, G. A. Piech, M. F. Gehrke, M. E. Lagus, L. W. Anderson, and C. C. Lin, "Electron impact excitation out of the metastable levels of argon into the $3p^5 4p$ $J = 3$ level," *Journal of Physics B*, vol. 29, no. 22, pp. L795–L800, 1996.

[31] J. B. Boffard, G. A. Piech, M. F. Gehrke, L. W. Anderson, and C. C. Lin, "Measurement of electron-impact excitation cross sections out of metastable levels of argon and comparison with ground-state excitation," *Physical Review A*, vol. 59, no. 4, pp. 2749–2763, 1999.

[32] G. A. Piech, J. B. Boffard, M. F. Gehrke, L. W. Anderson, and C. C. Lin, "Measurement of cross sections for electron excitation out of the metastable levels of argon," *Physical Review Letters*, vol. 81, no. 2, pp. 309–312, 1998.

[33] S. Ashida, C. Lee, and M. A. Lieberman, "Spatially averaged (global) model of time modulated high density argon plasmas," *Journal of Vacuum Science and Technology A*, vol. 13, no. 5, pp. 2498–2507, 1995.

[34] M. A. Lieberman and A. J. Lichtenberg, *Principles of Plasma Discharges and Materials Processing*, John Wiley & Sons, Hoboken, NJ, USA, 2nd edition, 2005.

[35] F. Kannari, M. Obara, and T. Fujioka, "An advanced kinetic model of electron-beam-excited KrF lasers including the vibrational relaxation in KrF^*(B) and collisional mixing of KrF^*(B,C)," *Journal of Applied Physics*, vol. 57, no. 9, pp. 4309–4322, 1985.

[36] J. H. Jacob and J. A. Mangano, "Modeling the KrF laser discharge," *Applied Physics Letters*, vol. 28, no. 12, pp. 724–726, 1976.

[37] J. H. Jacob and J. A. Mangano, "Total electron impact excitation cross sections of Ar and Kr," *Applied Physics Letters*, vol. 29, no. 8, pp. 467–469, 1976.

[38] M. Shaper and H. Scheibner, "Beitr," *Plasmaphys*, vol. 43, p. 1464, 1965.

[39] E. Eggarter, "Comprehensive optical and collision data for radiation action. II. Ar," *The Journal of Chemical Physics*, vol. 62, no. 3, pp. 833–847, 1975.

[40] A. Kaminska, B. Lopez, B. Izrar, and M. Dudeck, "Modelling of an argon plasma jet generated by a dc arc," *Plasma Sources Science and Technology*, vol. 17, no. 3, Article ID 035018, 2008.

[41] R. S. Devoto, "Transport coefficients of ionized argon," *Physics of Fluids*, vol. 16, no. 5, pp. 616–623, 1973.

[42] H. B. Milloy, R. W. Crompton, J. A. Rees, and A. G. Robertson, "The momentum transfer cross sections for electrons in ergon in the energy range 0–4 eV," *Australian Journal of Physics* , vol. 30, pp. 61–72, 1977.

[43] C. H. Chang and E. Pfender, "Nonequilibrium modeling of low-pressure argon plasma jets; part I: laminar flow," *Plasma Chemistry and Plasma Processing*, vol. 10, no. 3, pp. 473–491, 1990.

[44] J. J. Beulens, D. Milojevic, D. C. Schram, and P. M. Vallinga, "A two-dimensional nonequilibrium model of cascaded arc plasma flows," *Physics of Fluids B*, vol. 3, no. 9, pp. 2548–2557, 1991.

[45] R. S. Devoto, "Transport properties of ionized monatomic gases," *Physics of Fluids*, vol. 9, no. 6, pp. 1230–1240, 1966.

[46] G. M. W. Kroesen, D. C. Schram, C. J. Timmermans, and J. C. M. De Haas, "The energy balance of a plasma in partial local thermodynamic equilibrium," *IEEE Transactions on Plasma Science*, vol. 18, no. 6, pp. 985–991, 1990.

[47] K. Katsonis, S. Pellerin, and K. Dzierzega, "Collisional-radiative type modelling and application in plasma diagnostics," *High Temperature Material Processes*, vol. 7, no. 4, pp. 559–568, 2003.